Applied Physics B (2026) 132:59
https://doi.org/10.1007/s00340-026-08669-2

Applied Physics B
Lasers and Optics

RESEARCH

Single-shot polarization mapping of optical elements introducing spatially varying birefringence

Lyubomir I. Stoyanov[1,2] · Maria Mincheva[1] · Aleksander Stefanov[3,4] · Ivan Stefanov[1] · Alexander Dreischuh[1,2,5]

Received: 12 November 2025 / Accepted: 24 March 2026 / Published online: 9 April 2026

Abstract

Polarization mapping plays a key role in modern photonics, as many advanced optical applications, ranging from vector beam engineering to optical communication and material characterization, rely on precise knowledge of spatial polarization distributions. However, conventional mapping techniques often suffer from limitations such as multi-step measurements, sensitivity to misalignment, or the need for bulky setups, making single-shot and high-resolution polarization mapping particularly challenging. Here, we report a single-shot polarization mapping technique for parallel determination of the polarization change introduced by an unknown optical birefringent element or even device (e.g. *q*-plates, spatial light modulators). To achieve this, we used a 9×9 array of linearly polarized probe sub-beams to capture spatially resolved polarization information in a single measurement, allowing the two-dimensional polarization distribution to be reconstructed from just one data acquisition step. In this way, the measurement time is reduced while high spatial resolution is preserved. To demonstrate the robustness of the technique, we present a measurement with commercially available polarizing vortex plates, which convert linearly polarized light into radially or azimuthally polarized light, and the determination of the polarization response of a commercially available spatial light modulator. The main advantage of the method is its simplicity, achieved without sacrificing efficiency, which makes it readily accessible to any laboratory.

1 Introduction

Broadly defined, structured laser light is a beam whose amplitude, phase, and/or polarization are spatially modulated in a controlled way [1]. Without aiming for historical completeness, it is worth mentioning a few key articles in this field. Allen and co-authors introduced the concept of Laguerre-Gaussian beams carrying orbital angular momentum (OAM) [2]. Another work worth mentioning is a precise overview paper devoted to the OAM beams and structured light published by Padgett and co-authors in [3]. In contrast to phase optical vortices, which carry helical phase fronts, OAMa, and on-axis point singularities that result in donut-shaped intensity profiles [4–6], polarization vortices are characterized by different parts of the beam having different polarizations [7]. For example, in the radially polarized beams the electric field vectors point out from the beam axis, while for the azimuthally polarized beams they circulate around the beam axis. In both cases, the polarization singularity along the beam axis also leads to a circular transverse distribution of the beam's intensity. Highly structured laser beams with complex properties, denoted as vector vortex beams, can be generated by imprinting spatially varying

✉ Lyubomir I. Stoyanov
l.stoyanov@phys.uni-sofia.bg

Maria Mincheva
mariatm@uni-sofia.bg

Aleksander Stefanov
aleksander.a.stefanov@gmail.com

Ivan Stefanov
lambrev@phys.uni-sofia.bg

Alexander Dreischuh
ald@phys.uni-sofia.bg

[1] Department of Quantum Electronics, Faculty of Physics, Sofia University "St. Kliment Ohridski", James Bourchier Blvd. 5, Sofia 1164, Bulgaria

[2] National Centre of Excellence Mechatronics and Clean Technologies, Sofia, Bulgaria

[3] Institute of Mathematics and Informatics, Bulgarian Academy of Sciences, Sofia, Bulgaria

[4] Department of Mechatronics, Robotics and Mechanics, Faculty of Mathematics and Informatics, Sofia University "St. Kliment Ohridski", James Bourchier Blvd. 3, Sofia 1164, Bulgaria

[5] Bulgarian Academy of Sciences, Sofia, Bulgaria

polarization on phase optical vortices. Despite appearing complex at first, Liu and co-authors have shown [8] that vector vortex beam can be decomposed into a vector beam and an optical vortex. As a consequence, its generation can be realized by sequentially using a q-plate and a spiral phase plate. To avoid leaving the impression that these beams are of academic interest only, it should be noted that they also find application in high-resolution microscopy [9], material processing (since, e.g., they focus more tightly than Gaussian beams [10]), for increasing data capacity via OAM multiplexing (also called mode-division multiplexing (MDM), [11]), and in quantum optics [12], just to mention a few.

In this sense, optical elements introducing spatially varying birefringence due to their spatially varying optical axes orientations are very useful, especially if they can be reconfigured. Such elements are often denoted as q-plates [13, 14] or polarizing vortex plates. Essentially, the q-plate consists of an anisotropic liquid crystal film with a nonrandom local molecular orientation sandwiched between two glass plates [13]. An important parameter for such an element is the birefringent phase retardation of the film, which can be modulated by an applied external electric field [14]. Switching between suitable voltages can turn e.g. a left (right) circular polarization beam with zero OAM into a right (left) circular polarization beam with OAM equal to $2q\hbar$ (or to $-2q\hbar$) [13]. Other highly flexible devices used in the experimental practice for generating (phase-)structured beams are the liquid crystal spatial phase modulators (SLMs). The SLMs are however polarization-sensitive devices [15], and their polarization characterization is of undoubted interest (see e.g. [16]). When switched off, the reflective phase-only SLM is acting as a mirror. When turned on and not programmed with any phase distribution, it should not alter the beam's polarization, provided that the input polarization is aligned along the optical axis of the liquid crystal molecules. For angles of incidence less than 10° the retardance dependence on this angle is expected to have negligible effect on the phase modulation response of the display [17].

To precisely estimate any potential changes in the beam's polarization caused by the SLM or other birefringent elements, polarization mapping techniques can be employed. Polarization mapping refers to the measuring and visualizing the spatial distribution of the polarization state across a light beam. It reveals how polarization varies from point to point in space showing, e.g., regions with radial, azimuthal, or elliptical polarization [18–20]. Single-shot determination of spatially varying polarization states of light in time is important in many fields of physics, medical diagnostics, industrial manufacturing, and product quality assurance (see e.g. [21, 22] and the references therein).

Looking towards the field of the snapshot polarimetry, without any claim for completeness, we will mention some of the recent achievements. In [21] it is shown that the space-varying geometric phase and the space-varying contrast of the interference pattern obtained using a polarized reference light beam can provide complete information on the spatially varying polarized light. This is achieved in a Mach-Zehnder interferometric arrangement by recovering spatially varying polarized light generated by a SLM. In [23] a single-path setup is presented, composed by a SLM and a tunable retarder. The authors demonstrate spatial polarization modulation of the input beam for interferometer-free probing of the medium's polarization characteristics. The four Stokes parameters (corresponding to a sum or difference of measurable intensities) precisely describe the polarization state of the electromagnetic (optical) waves. Generally, the simultaneous recording of the Stokes parameters using cameras relies on one of the following approaches – division of amplitude (DoA) or division of focal plane (DoFP). In the DoA imaging approach, multiple synchronized cameras are used, each one with its own polarization element, as well as beam splitters to form the distinct channels [24]. Again in [24], the authors report a technique based on a homogeneous dispersive retarder placed before a polarization sensor to harness wavelength-dependent retardation, thus enabling the differentiation of polarization states across the sensor's color channels. Assuming weak wavelength dependence of polarization for incoming light, this method facilitates the real-time, simultaneous measurement of the complete Stokes vector of incident light as well. In [25], using the DoFP approach, the authors demonstrate a single-shot full-Stokes imaging polarimeter. In essence, it consists of color polarization sensors composed by on-chip lens array, four color filters and sets of four identical micro wire-grid polarizers behind each filter, all packaged on top of the camera sensor. The device is shown to be able to capture local intensity, color, and polarization of a 2-D optical field in a single shot of measurement. Even through still challenging to design and expensive to produce, polarization arrays based on metasurfaces, offer an alternative approach by employing polarization sensitive metasurfaces to direct light to different pixels on an image sensor according to various polarization bases [26, 27]. Another interesting work worth mentioning here is [28]. Here the authors demonstrated a single-shot full-Stokes polarimeter based on a disordered twisted nanohole array in a combination with a deep learning algorithm.

In this paper we focus on an elegant single-shot approach to map the polarization distribution introduced by optical elements with spatially varying birefringence. A key element in the experimental setup is a diffractive optical element (DOE) that transforms the incident (Gaussian) laser beam into an ordered array of 9×9 (Gaussian) subbeams with nearly equal power and identical polarization.

The polarization (e.g. linear) of each of the 81 sub-beams changes depending on the birefringent properties of the medium/element and the specific point/region through which the individual sub-beam passes. The optical scheme ends in the classic way – with an analyzer and a CCD camera. The local change in the polarization is determined by the local change in the peak intensity of the sub-beams. For a precise birefringence measurement with increased number of points one can either use a denser array or use a DOE that can be rotated stepwise in a controlled manner (however at the cost of giving up the single-shot mode). The simplicity of the presented optical scheme and the requirement for only one distinct yet commercially available element make the method accessible to any laboratory. The single-shot mode of operation is especially valuable in situations where the birefringence changes within timescales of the order of and longer than the response time of the used CCD camera. In our case the fluctuations of the sub-beams in space and time are averaged over the exposure time of the detector only (typically within 125 ms $= (1/8)$ s for the cases reported here). In our view, this method is straightforward, yet accurate and cost-effective alternative to commercially available birefringence imaging systems suitable for measuring e.g. space-varying dynamic stress-induced birefringence.

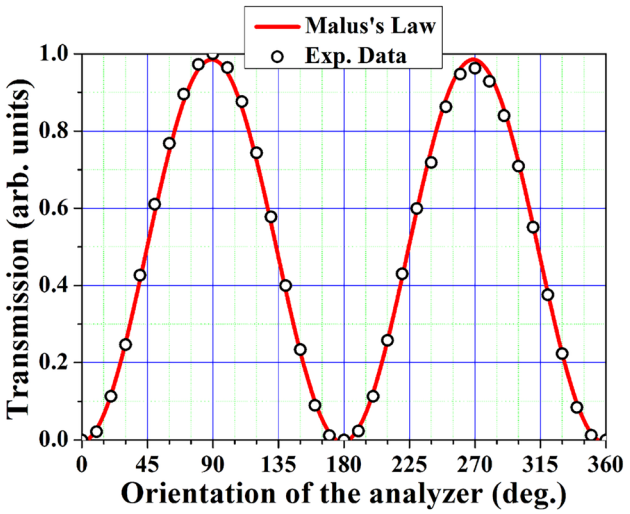

Fig. 1 Test for the quality of the used analyzer and for the degree of polarization of the laser beam. Hollow circles – recorded transmission of the analyzer illuminated with the linearly polarized beam of a Nd:YVO_4 laser at 532 nm when changing the orientation of the analyzer in $10°$-steps. Red solid curve – the $\cos^2(\alpha + 45°)$ function corresponding to the Malus's law (in this case – at a constant angular offset of $45°$)

2 Experimental setup and results

2.1 Experimental scheme and test results

The initial phase of this analysis involves testing the polarization of the used continuous-wave laser (Nd:YVO_4 laser with an intracavity generation of a second harmonic, emitting at a wavelength of 532 nm) and the available analyzer (LPVISE100-A, Thorlabs). As known, according to the Malus's law the intensity of the light transmitted by the analyzer must vary as the square of the cosine of the angle between the plane of polarization of the laser beam and the transmission plane of the analyzer. In Fig. 1, the hollow circles represent the transmission of the analyzer as its orientation monotonically changes in $10°$-steps. Red solid curve in the same figure is the $\cos^2(\alpha + 45°)$ function corresponding to the Malus's law, where α is the angle of orientation of the analyzer. (The constant angular offset of $45°$ is just visually shifting the data/curve and has no other physical meaning). The good agreement between the experimental data and the theoretical curve indicates that the used laser beam and the analyzer have high degree of polarization (>100:1 for the laser according to the manufacturer's data sheet) and reliable analyzing properties (extinction ratio >1000:1). With this in mind, Fig. 2a shows the first experimental setup designed to realize the so-called trivial beam multiplication.

The purpose of this setup (see Fig. 2a) is to introduce and visualize to the reader the expected behavior of the used diffractive optical element (DOE, MS-254-Q-Y-A, HOLO/OR) and commercially available vortex polarization plates (q-plates, WPV10L-532 and WPV10-532, Thorlabs). Briefly, the linearly polarized Gaussian laser beam passes through the test plate (TP; vortex polarization plate) and, depending on its type, is transformed into either polarization optical vortex (OV) of order q=1 or into OV of order q=2 (here q denotes the order of the obtained polarization vortex beam). The DOE simply replicates this single vortex beam into a 9×9 array of secondary OV beams with q=1 (frame (b) in Fig. 2) or into array of OVs of order q=2 ((frame (c) in Fig. 2)). As the secondary array of beams is divergent, a focusing lens L with a suitable focal length should be used to collimate it. In our case, lens with a focal length $f = 15$ cm is chosen so that the parallel array of secondary beams correctly maps onto the CCD camera's photodiode matrix (1600×1200 pixels, each of size 4.4 μm × 4.4 μm). If an analyzer is placed in front of the CCD camera, depending on its orientation, it will transmit only the components of the field corresponding to its orientation. Fig. 2 shows the power density distributions of the polarization vortices behind the rotating analyzer RA positioned at $0°$, $45°$, $90°$, and $135°$, for polarization charges q=1 (frames (b1)-(b4)) and for q=2 (frames (c1)-(c4)), respectively. The results

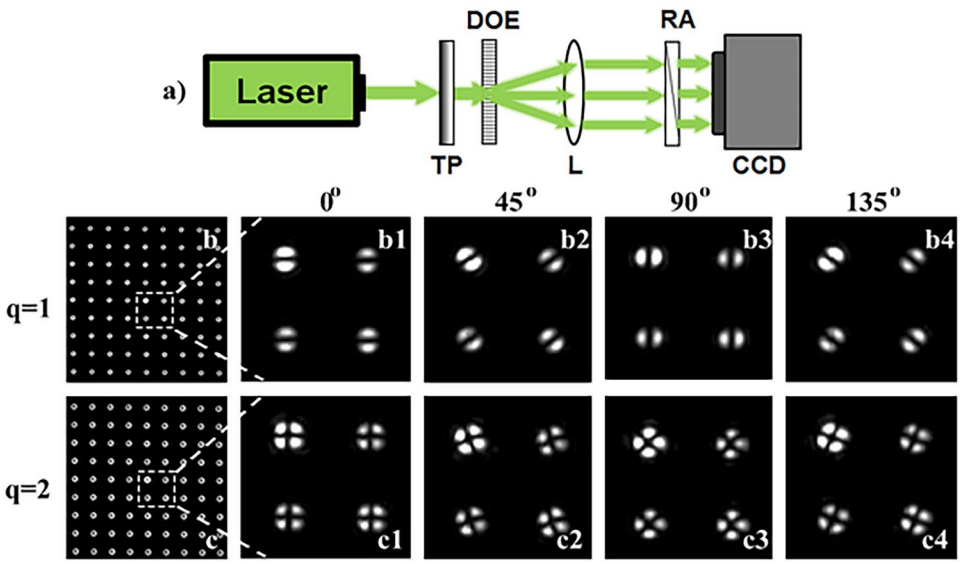

Fig. 2 **(a)** Experimental setup for trivial beam multiplication showing the expected behavior of the used DOE. TP – test birefringent plate generating polarization OVs of orders q=1 or q=2. DOE – diffractive optical element creating an array of 9×9 identical secondary beams. L – thin lens ($f = 15$ cm). RA – Rotating analyzer. CCD – charge-coupled device camera. **(b)** and **(c)** – multiplication of polarization OVs of orders q=1 (b) and q=2 (c) in a 9×9 array. Dashed rectangle – 4 OVs analyzed by rotating the RA in 45°-steps (see (b1-b4) for q=1 and (c1-c4) for q=2)

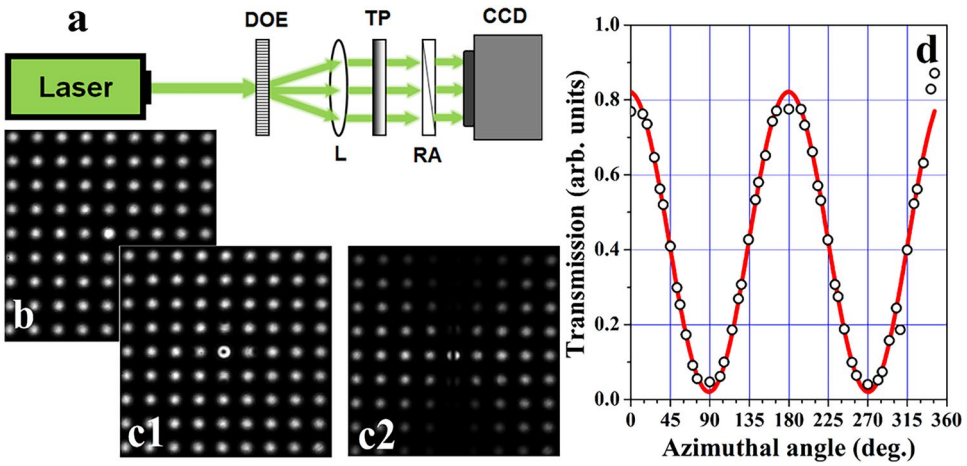

Fig. 3 **(a)** – Experimental setup for the single-shot polarization mapping of a commercially available polarizing plate of order q=1 used as a test plate (TP). The DOE and the L create a collimated array of 9×9 array of identical, linearly polarized (Gaussian) test sub-beams (panel **(b)**) probing different areas of the TP. **(c1)** – CCD image of the 9×9 array recorded after passing through the TP, but without being analyzed by the RA. **(c2)** – The polarization state of all beams is determined within a single shot using a stationary analyzer RA and a CCD camera. **Graph (d)** – Retrieved transmission after the stationary analyzer vs. azimuthal angle

agree with the data known from the literature and are also illustrated in Fig. S1 of the Supplementary material to the paper.

2.2 Single-shot mapping of polarization plates with q=1 and q=2

Panel (a) of Fig. 3 shows the modified experimental setup for single-shot polarization mapping in the case where the polarization vortex plates are probed by the 9×9 array of secondary beams. Even though these are commercially available polarizing plates with a known liquid crystal orientation, we aim to demonstrate the robustness of the discussed single-shot technique by testing elements with known polarization behavior before applying it to an unknown birefringent element.

In more details, the linearly polarized Gaussian laser beam passes through the diffractive optical element DOE and is split into 9×9 identical linearly polarized secondary beams. In Fig. 3(b) all test beams are shown after collimation with a lens of focal length $f = 15$ cm as projected on the CCD camera chip without passing through a test element. The beamlet spacing in the reported data is 0.8 mm, the spot size – 107 μm. It can be reduced by using commercially available DOEs generating denser array of e.g. 51×51 sub-beams (model MS-805-I-Y-A; HoloOr) or even 201×201 sub-beams (model MS-835-J-Y-X; HoloOr). An alternative approach is to use a focusing lens of a shorter

focal length, leading to a smaller offset between the sub-beams of the array.

Figure 3(c1) shows the result when the 9×9 array of identical beams is transmitted through the test plate (TP). The TP creates a polarization OV of order q=1. The central beam of the array clearly shows a ring-shaped power density distribution, which is an indication of the presence of a singularity. (This result alone, however does not reveal whether the effect arises from polarization or phase singularity.) Let us now align the rotation analyzer (RA) in the setup. We continue to call it RA since it can, in principle, rotate, but remains stationary during each measurement to allow for a single-shot data acquisition. Figure 3(c2) shows the 9×9 array of test polarization-modulated sub-beams after passing through the RA and captured by the CCD camera in a single frame. Each secondary beam, passing through the stationary analyzer is transmitted differently, meaning that each test sub-beam changed its polarization state depending on the local birefringence of the tested plate. The central ring-shaped beam from Fig. 3(c1) is now transformed into a structure resembling the Hermite–Gaussian mode HG_{01}, indicating the presence of a polarization singularity rather than a phase dislocation (see Supplementary material for further details). The changes in the transmission of the remaining test sub-beams (Fig. 3(c2)) follow the Malus's law. All this confirms the expected behavior of the tested element (WPV10L-532 – q-plate generating a polarization OV of the order q=1).

In all presented measurements, the central peak from the 9×9 array was aligned to be modulated by a polarization/phase singularity. The plates used to generate polarization vortices, and the spatial phase distributions of the phase vortices on the SLM (see Sect. 2.3), were expected to modulate the signal azimuthally, not radially. Assuming this, the secondary beams falling within the same radial cross-section (i.e., under the same azimuthal angle) were averaged in intensity, and the data in the graphs are presented as a function of the azimuthal angle. To graphically visualize the potential phase shift due to spatially dependent birefringence, we compared the experimental data with Malus's law. Generally, for more complex distributions of birefringence, the complete characterization of the polarization state must be achieved by measuring the Stokes parameters and visualizing them accordingly.

Before recording the intensity distribution behind the analyzer, we paid attention to ensure that none of the secondary beams of the 9×9 array is saturated. The relatively weak ($< \pm 5\%$) fluctuations in the intensities of these beams originating from the used diffractive optical element could be considered by normalizing the particular data recorded after the analyzer to reference data recorded without any test plate. We refrained from doing so, adhering to single-shot data acquisition.

In Fig. 3(d), with hollow circles we show the retrieved transmission for each individual peak of the array presented in Fig. 3(c2) after analyzed by the RA as a function of the azimuthal angle. Here, the 'azimuthal angle' is defined as the angle through which an imaginary horizontal line, starting from the center of the structure and pointing to the right is rotated counter-clockwise to pass through the selected test peak. This method of determining the azimuthal angle at which each sub-beam is 'mapped' explains the somewhat uneven distribution of experimental points along the curve in Fig. 3(d). The number of these experimental points (marked with hollow circles on the graph) is obviously less than 81, since at some angles of rotation relative to the horizontal line, there is more than one test sub-beam. For this reason, we plotted on the graph the average value of their transmitted signals. The motivation behind such data processing is the preliminary information for the test plate which generates a polarization vortex. Let us remind that for such a test plate, the expectation is that the birefringence in the radial direction from the center of the plate will always be the same [29] (and will change only in the azimuthal direction).

In Fig. 4, following the same manner of presentation, we show results from the single-shot mapping of a commercially available polarization vortex plate (OV of order q=2) used again as a test plate. In panels (a1)-(a3) of Fig. 4 we show the power-density distributions of the 81 sub-beams with locally modulated polarizations after passing through the analyzer RA and recorded by the CCD camera, for three different orientations of the RA – $0°$, $45°$, and $90°$, respectively. In each frame, the central peak of the array is split into 4 sub-peaks and resembles a Hermite-Gaussian mode HG_{11}. This central structure rotates with rotating the RA, as can be expected when analyzing a polarization vortex of order q=2. The central structures shown in Fig. 4(a1) and (a3) can be compared with the theoretically generated square amplitude moduli of an optical vortex with polarization order q=2 in two mutually perpendicular directions. This is also shown in Fig. S1 of the Supplementary material. The graph in Fig. 4(b) shows the retrieved transmission of the sub-beams after the RA is kept at $0°$ (i.e. from the data shown in Fig. 4(a1)). Hollow circles denote the experimental data, while the red solid curve is a plot of the function $\cos^2$(Azimuthal angle), where the azimuthal angle is defined as above. Although the experimental points appear more sparsely distributed as compared to these in Fig. 3(d), this is merely a result of the larger number of peaks in the curve. The comparison of the central structures in Fig. 4(a1) and (a3) and the frames (d2) and (e2) in Fig. S1 in the Supplementary material, as well as the four peaks in the graph

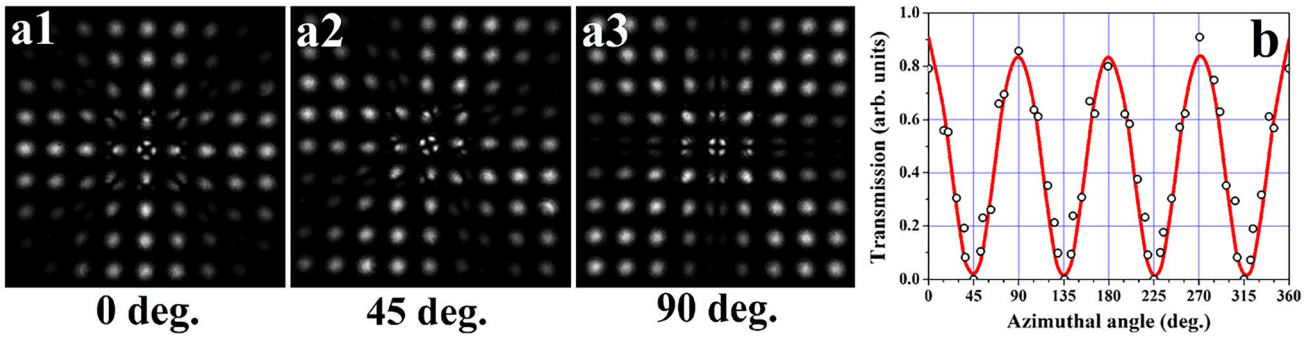

Fig. 4 (a1)-(a3) – Energy-density distributions of the 81 sub-beams with locally modulated polarizations after passing through the analyzer RA and recorded by the CCD camera for three different orientations of the RA. **Graph (b)** – Retrieved transmission of the sub-beams after the RA is kept at 0° (see frame (a1))

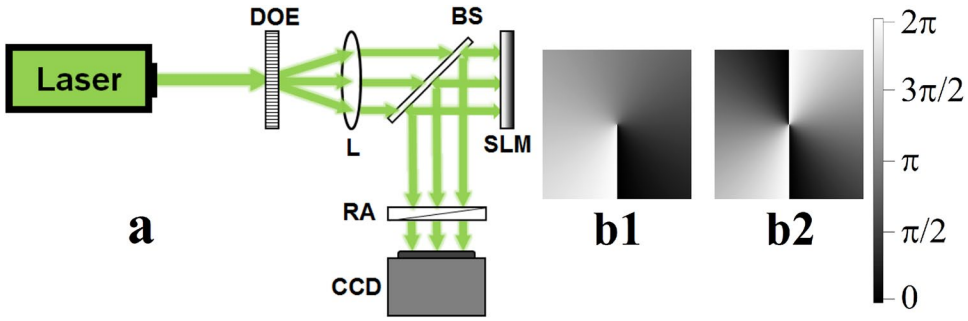

Fig. 5 (a) – Experimental setup for single-shot polarization mapping of a reflective SLM (used as a birefringent samples). The introduced non-polarizing beam splitter (BS) redirects part of the reflected signal from the spatial light modulator (SLM) to the analyzer RA and the CCD camera. **(b1)** and **(b2)** – Phase profiles of a phase OV with a topological charge l=1 and l=2, respectively

in Fig. 4(b) confirm that the tested birefringent plate creates a polarization vortex of order q=2. The polarization behind the TP changes azimuthally, remaining constant in radial direction when the azimuthal angle does not change. To summarize the results presented so far, the tested optical elements demonstrated the expected performance when studied with the suggested polarization mapping technique. An increased number of independent spatial samples can be obtained by giving up the single-shot mode of the operation, controllably azimuthally rotating the array of sub-beams to $(1/n)$-th of the angular spacing between two sub-beams thus achieving more experimental points and smoother curves.

2.3 Polarization mapping of the LCoS display of a spatial light modulator

In Fig. 5(a) we show the modified experimental setup for single-shot polarization mapping of reflective birefringent elements (in this case a reflective spatial light modulator). It is similar to this shown in Fig. 3(a). The only difference is the aligned non-polarizing beam splitter redirecting part of the reflected signal from the spatial light modulator (SLM) to the analyzer RA and the CCD camera. The SLM is commercially available, built using the Liquid-Crystal-on-Silicon (LCoS) technology. It has an active area of 15.36 mm × 8.64 mm (nominal resolution 1920 × 1080 pixels), pixel pitch 8.0 μm, fill factor of 93% and an image frame rate of 60 Hz. The DOE-to-L and the L-to-CCD camera distances are kept the same as in the setup presented in Fig. 3(a). For the following measurements, we programmed the SLM with the phase distributions of OVs of different topological charges l. Panel (b1) in Fig. 5 shows the spiral phase of an OV with l=1, while panel (b2) – the spiral phase of OV with l=2. When the SLM is programmed with such phase distributions, the point phase dislocations cause amplitude modulation of the input Gaussian beam with an initially smooth wavefront which results in the generation of phase optical vortex. More detailed information on this is given in Fig. S2 in the Supplementary material. In general, liquid crystal phase modulating SLMs could suffer from crosstalk between adjacent pixels. The pixel crosstalk is caused by voltage changes across the border of neighboring pixels and by elastic forces in the liquid crystal material preventing spatial variations in the phase modulation (see e.g. [30, 31] and the references therein). As a result, the actual phase modulation of a pixel depends on the voltage applied to the neighboring pixels. On the other hand, pixels near the physical edges of the SLM display suffer from asymmetry of their surroundings which are different for pixels near the central part of the display. In our measurements we deliberately avoided positioning of sub-beams near the edges of the SLM display. Additionally, when more than one sub-beam was located along the same radial cross-section (i.e., under the same azimuthal angle), they were averaged in intensity, thus reducing the potential influence of the SLM's peripheral areas. The used spiral phase distributions in the

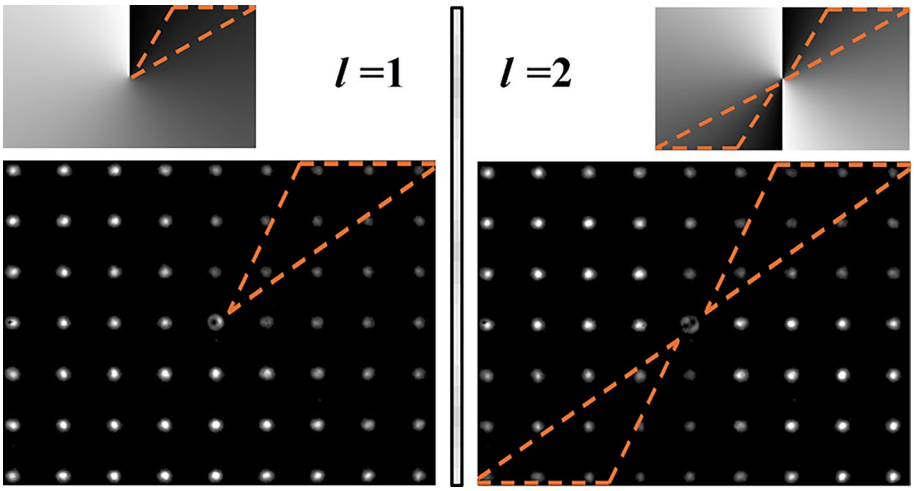

Fig. 6 **Upper frames** – phase distributions of a singly-charged OV (l=1, left) and of a two-fold charged OV (=2, right) encoded on the tested reflective phase-only SLM. **Lower frames** – arrays of sub-beams (initially linearly polarized Gaussian beams) after reflection from the SLM, transmission through the analyzer (RA), and final capture by the CCD camera, for OVs with l=1 (left array) and l=2 (right array). The orange dashed sectors are intended to mark intervals of greyscale levels on the phase distributions and regions on the SLM which non-negligibly rotate the polarizations of the probe sub-beams

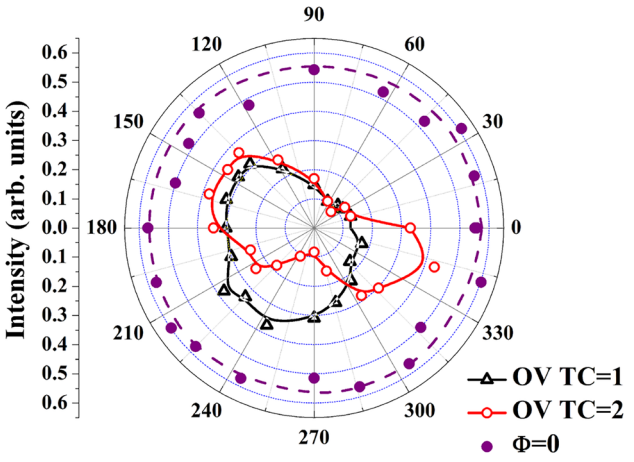

Fig. 7 Polar plot of the angular distribution of the reflected signal from the SLM retrieved from a single-shot when programming the SLM with the phases of OVs with topological charges l=1 (black open triangles) and l=2 (red open circles). The black/red solid curves are intended to guide the eye underlying the well pronounced azimuthal asymmetry of the curves. Purple solid dots – recorded data when the SLM is switched off thus acting as a mirror, introducing a constant phase. Purple dashed circle – the theoretically ideal case of no birefringence

presented experiment do not contain high spatial frequencies (i.e. frequent abrupt phase changes) except the 0-2π transition. Our approach for compensating the crosstalk in this specific region relies on fine tuning the "dark and bright voltage" making phase 0 and 2π indistinguishable and thus no radial modulation is observed in the intensity distribution of the optical vortex. Other methods are discussed in [30] where the authors use iterative algorithms to compensate for the crosstalk effects, which are unfortunately not applicable for single-shot measurements.

Figures 6 and 7 summarize the results obtained with the reflective phase-only SLM. It displayed unexpected birefringent properties. The phase distributions shown in the upper row of Fig. 6 are asymmetric in size matching the rectangular full HD array of liquid crystal pixels. The phase distribution shown in the upper left frame in Fig. 6 was used to generate optical vortices with topological charge l=1 in the reflected beam, while the phase distribution in the upper right frame was used for optical vortices with topological charge l=2. Although not related to the present analysis, we would like to mention that pure phase modulation with point phase singularities and spiral phases leads to amplitude modulations in the reflected beams, characteristic for the optical vortices (sometimes referred to as “donut-shaped beams”). In Fig. S2 in the Supplementary material to this paper we show more information regarding the generation of phase optical vortices. The essential (raw) experimental data are shown in the bottom two panels of Fig. 6. They demonstrate the modulation of the arrays of sub-beams (initially linearly polarized Gaussian beams), after they are simultaneously reflected from the SLM (encoded with a vortex phase distribution), then transmitted through the analyzer RA, and finally captured by the CCD camera.

Let us take a closer look at the *lower left* frame of Fig. 6, captured when the SLM is programmed with the phase distribution of OV with topological charge l=1. The phase varies once from 0 to 2π in the azimuthal direction, around the vortex axis. The point phase dislocation is in the center. The result of its presence is the optical vortex, which can be seen in the central sub-beam of the array. All other sub-beams of the array do not carry any phase dislocations but occupy areas with different phase values. Since the sub-beams are much narrower than the aperture of the modulator, we can assume that the phase across each sub-beam is almost constant, but different for the different sub-beams (depending on the programmed grey level). Surprisingly, after passing through the stationary analyzer (RA) the sub-beams reveal a position-dependent birefringence. Particularly pronounced is the decrease in the intensities of the sub-beams within the area of the sectors outlined with a orange dashed triangle in the left frames of Fig. 6.

The *lower right* frame in Fig. 6 represents the case when the SLM was programmed with the phase distribution of an optical vortex with topological charge l=2 (see the upper right frame in the same figure). The central ring-shaped beam from the array carrying the vortex with topological charge 2 is particularly interesting. Since OVs with higher topological charges are more sensitive to weak modulations [32] (e.g., from incident continuous radiation, weak reflections, asymmetry relative to the axis of the carrier sub-beam, or pixel cross-talk), the double-charged vortex has decayed into two singly-charged vortices with well-separated dark cores. For the rest sub-beams forming the array is observed similar behavior as for the case of the mapping of l=1. Here, for l=2, however, the spatially distributed birefringence is mapped differently by the sub-beams, as seen by their noticeably different intensities after passing through the analyzer (RA). In this case, two areas with reduced peak intensities are visible and marked by orange dashed triangles.

Important conclusion drawn from the data is that even at normal incidence (well below the 10° limit reported in [17]) the tested liquid crystal phase-only SLM introduces non-negligible birefringence. It is important to emphasize that the observed spatially distributed birefringence refers to the spatially varying birefringence arising from the spatially distributed electrical signals applied to the liquid crystal pixels to achieve the desired phase profile.

Figure 7 visualizes graphically the results obtained in Fig. 6. The polar plot shows the angular distribution of the reflected signal from the SLM retrieved from a single-shot when the SLM is switched off (solid purple dots) and when programmed with the phase distributions of OVs with topological charges l=1 (black open triangles) and l=2 (red open circles). When the SLM is switched off, it is acting as a mirror introducing a constant phase shift. The purple dashed circle represents the theoretically ideal case of no birefringence. Unfortunately, it can be seen that at a constant phase the experimental points are not located exactly on the purple circle. This is because the used DOE generates an array of 9×9 sub-beams with slightly different peak intensities (variation typically below $< \pm 5\%$). (Of course, the recorded intensities of the sub-peaks in the presence of birefringence could be normalized to the unperturbed peak intensities, but we refrained from doing that.) The black/red solid curves connecting the points are intended to guide the eye only, underlying the azimuthal asymmetry of the curves. Azimuthal asymmetry of the signals transmitted through the analyzer means that the signals reflected from the SLM are with changed polarizations. For l=1, the polar plot in Fig. 7 shows an one-sided 'flattening' of the curve, which is, roughly speaking, D-shaped. At l=2, there are two 'tightenings' and the curve resembles the number 8. These 'tightenings' are at different places along the modulator aperture and, therefore, are not due to its local features, but are a characteristic of the modulator's response to specific voltages applied to reorient the liquid crystals.

3 Conclusion

In this study, we presented a simple yet effective technique for simultaneous (single-shot) mapping of the polarization changes induced by birefringent optical elements including the polarization response of reflective (or transmissive) phase-only spatial light modulators. This is achieved using the combination of a diffractive optical element generating arrays of 9×9 secondary linearly polarized Gaussian sub-beams, an analyzer and a CCD camera. If the spatially dependent change in the polarization is constant in time, more experimental data can be derived per curve, simply by abandoning the single-shot mode and rotating the diffractive optical element to a second or to more positions. If the polarization change is relatively slow (longer than the time it takes for the used camera to capture more frames) the single-shot mode would allow mapping of birefringence in both space and time. In this sense, we believe that we have demonstrated a straightforward and effective approach for single-shot polarization mapping, that can be modified for measuring dynamic space-varying birefringence.

Supplementary Information The online version contains supplementary material available at https://doi.org/10.1007/s00340-026-08669-2.

Acknowledgements The authors gratefully acknowledge funding of the Bulgarian National Science Fund (project КП-06-H78/6). This work was also supported by the Bulgarian Ministry of Education and Science as a part of the National Roadmap for Research Infrastructure, project ELI ERIC BG and by the European Regional Development Fund under "Research Innovation and Digitization for Smart Transformation" programme 2021–2027 under Project BG16RFPR002−1.014-0006 "National Centre of Excellence Mechatronics and Clean Technologies". M.M., L.S. and A.D. were also supported by the European Union NextGenerationEU through the 'National Recovery and Resilience Plan of the Republic of Bulgaria, project BG-RRP−2.004-0008-C01'.

Author Contributions Conceptualization, L.S. and A.D.; methodology, L.S.; validation, M.M. and I.S.; investigation, L.S., M.M. and A.S.; writing - original draft preparation, A.D.; writing - review and editing, L.S., I.S., and A.D.; visualization, A.S.; supervision, A.D. All authors have read and agreed to the submitted version of the manuscript.

Data Availability The datasets generated and analyzed during the current study are available from the corresponding author upon a reasonable request.

Declarations

Conflict of interest/Conflict of interest The authors declare no conflict of interest.

Conflict of interest The authors declare no conflict of interest.

References

1. H. Rubinsztein-Dunlop, A. Forbes, M.V. Berry, M.R. Dennis, D.L. Andrews, M. Mansuripur, C. Denz, C. Alpmann, P. Banzer, T. Bauer, E. Karimi, L. Marrucci, M. Padgett, M. Ritsch-Marte, N.M. Litchinitser, N.P. Bigelow, C. Rosales-Guzmán, A. Belmonte, J.P. Torres, T.W. Neely, M. Baker, R. Gordon, A.B. Stilgoe, J. Romero, A.G. White, R. Fickler, A.E. Willner, G. Xie, B. McMorran, A.M. Weiner, Roadmap on structured light. J. Opt. **19**(1), 013001 (2016). https://doi.org/10.1088/2040-8978/19/1/013001
2. L. Allen, M.W. Beijersbergen, R.J.C. Spreeuw, J.P. Woerdman, Orbital angular momentum of light and the transformation of Laguerre-Gaussian laser modes. Phys. Rev. A **45**, 8185–8189 (1992). https://doi.org/10.1103/PhysRevA.45.8185
3. M. Padgett, J. Courtial, L. Allen, Light's orbital angular momentum. Phys. Today **57**(5), 35–40 (2004). https://doi.org/10.1063/1.1768672
4. Y.S. Kivshar, B. Luther-Davies, Dark optical solitons: physics and applications. Phys. Rep. **298**(2), 81–197 (1998). https://doi.org/10.1016/S0370-1573(97)00073-2
5. M.R. Dennis, K. O'Holleran, M.J. Padgett, Chapter 5 singular optics: Optical vortices and polarization singularities. Progress in Optics, vol. 53, pp. 293–363. Elsevier (2009). https://doi.org/10.1016/S0079-6638(08)00205-9
6. L. Stoyanov, S. Topuzoski, G.G. Paulus, A. Dreischuh, Optical vortices in brief: introduction for experimentalists. Europ. Phys. J. Plus **138**(8), 702 (2023). https://doi.org/10.1140/epjp/s13360-023-04227-3
7. Q. Zhan, Cylindrical vector beams: from mathematical concepts to applications. Adv. Opt. Photon. **1**(1), 1–57 (2009). https://doi.org/10.1364/AOP.1.000001
8. Z. Liu, Y. Liu, Y. Ke, Y. Liu, W. Shu, H. Luo, S. Wen, Generation of arbitrary vector vortex beams on hybrid-order Poincaré sphere. Photon. Res. **5**(1), 15–21 (2017). https://doi.org/10.1364/PRJ.5.000015
9. M.G.L. Gustafsson, Surpassing the lateral resolution limit by a factor of two using structured illumination microscopy: Short communication. J. Microsc. **198**(Pt 2), 82–87 (2000). https://doi.org/10.1046/j.1365-2818.2000.00710.x
10. X. Hao, C. Kuang, T. Wang, X. Liu, Phase encoding for sharper focus of the azimuthally polarized beam. Opt. Lett. **35**(23), 3928–3930 (2010). https://doi.org/10.1364/OL.35.003928
11. J. Wang, J.Y. Yang, I.M. Fazal, N. Ahmed, Y. Yan, H. Huang, Y. Ren, Y. Yue, S. Dolinar, M. Tur, A.E. Willer, Terabit free-space data transmission employing orbital angular momentum multiplexing. Nat. Photonics **6**, 488–496 (2012). https://doi.org/10.1038/nphoton.2012.138
12. J. Tang, Y. Ming, Z. Chen, W. Hu, F. Xu, Y. Lu, Entanglement of photons with complex spatial structure in Hermite–Laguerre–Gaussian modes. Phys. Rev. A **94**, 012313 (2016). https://doi.org/10.1103/PhysRevA.94.012313
13. A. Rubano, F. Cardano, B. Piccirillo, L. Marrucci, Q-plate technology: a progress review. J. Opt. Soc. Am. B **36**(5), 70–87 (2019). https://doi.org/10.1364/JOSAB.36.000D70
14. O. Krupych, T. Dudok, I. Skab, Y. Nastishin, Z. Hrabchak, A. Chernenko, O. Buluy, P. Zelenov, V. Nazarenko, O. Kurochkin, R. Vlokh, Electric field controlled switching of an optical vortex charge with a liquid crystal cell. Opt. Commun. **579**, 131593 (2025). https://doi.org/10.1016/j.optcom.2025.131593
15. J.E. Wolfe, R.A. Chipman, Polarimetric characterization of liquid-crystal-on-silicon panels. Appl. Opt. **45**, 1688–1703 (2006). https://doi.org/10.1364/AO.45.001688
16. V. Tiwari, S.K. Gautam, D.N. Naik, R.K. Singh, N.S. Bisht, Characterization of a spatial light modulator using polarization-sensitive digital holography. Appl. Opt. **59**, 2024–2030 (2020). https://doi.org/10.1364/AO.380572
17. A. Lizana, N. Martin, M. Estapé, E. Fernández, I. Moreno, A. Márquez, C. Iemmi, J. Campos, M.J. Yzuel, Influence of the incident angle in the performance of Liquid Crystal on Silicon displays. Opt. Express **17**, 8491–8505 (2009). https://doi.org/10.1364/OE.17.008491
18. X. Wang, F. Yang, J. Yin, Mapping the polarization distribution of arbitrary vector polarization beam. Optik **144**, 124–131 (2017). https://doi.org/10.1016/j.ijleo.2017.06.081
19. B. Schaefer, E. Collett, R. Smyth, D. Barrett, B. Fraher, Measuring the Stokes polarization parameters. Am. J. Phys. **75**, 163–168 (2007). https://doi.org/10.1119/1.2386162
20. J. Yang, D. Lin, D. Bao, S. Tao, Pixel level control of amplitude, phase, and polarization of an arbitrary vector beam. Appl. Phys. Lett. **121**, 191103 (2022). https://doi.org/10.1063/5.0090177
21. B.S. Athira, M. Pal, S. Mukherjee, J. Mishra, D. Nandy, N. Ghosh, Single-shot measurement of the space-varying polarization state of light through interferometric quantification of the geometric phase. Phys. Rev. A **101**, 013836 (2020). https://doi.org/10.1103/PhysRevA.101.013836
22. N. Shitrit, I. Yulevich, E. Maguid, D. Ozeri, D. Veksler, V. Kleiner, E. Hasman, Spin-optical metamaterial route to spin-controlled photonics. Science **340**(6133), 724–726 (2013). https://doi.org/10.1126/science.1234892
23. E. Grigoryan, A. Sargsyan, T. Sarukhanyan, M. Rafayelyan, Single-path spatial polarization modulation for vector transmission matrix measurement and polarization control in scattering media. Photonics **12**(11), 142 (2025). https://doi.org/10.3390/photonics12111145
24. S. Bian, O. Arteaga, A simple pathway for complete polarization vision. Sci. Rep. **15**(1), 8885 (2025). https://doi.org/10.1038/s41598-025-92653-x
25. X. Tu, S. McEldowney, Y. Zou, M. Smith, C. Guido, N. Brock, S. Miller, L. Jiang, S. Pau, Division of focal plane red-green-blue full-Stokes imaging polarimeter. Appl. Opt. **59**(22), 33–40 (2020). https://doi.org/10.1364/AO.391027
26. Y. Intaravanne, X. Chen, Recent advances in optical metasurfaces for polarization detection and engineered polarization profiles. Nanophotonics **9**(5), 1003–1014 (2020). https://doi.org/10.1515/nanoph-2019-0479

27. A. Basiri, X. Chen, J. Bai, P. Amrollahi, J. Carpenter, Z. Holman, C. Wang, Y. Yao, Nature-inspired chiral metasurfaces for circular polarization detection and full-Stokes polarimetric measurements. Light Sci. Appl. **8**(1), 78 (2019). https://doi.org/10.1038/s41377-019-0184-4
28. M. Wu, L. Huangchen, W. Ma, S. Huang, S. Hou, X. Yang, J. Du, J. Peng, Y. Hou, High-performance single-shot full-Stokes polarimetry based on long-range disorder moiré metasurface. Opt. Express **34**(5), 7715–7728 (2026). https://doi.org/10.1364/OE.587906
29. M. Aizawa, M. Ota, K. Hisano, N. Akamatsu, T. Sasaki, C.J. Barrett, A. Shishido, Direct fabrication of a q-plate array by scanning wave photopolymerization. J. Opt. Soc. Am. B **36**(5), 47–51 (2019). https://doi.org/10.1364/JOSAB.36.000D47
30. M. Persson, D. Engström, M. Goksör, Reducing the effect of pixel crosstalk in phase only spatial light modulators. Opt. Express **20**(20), 22334–22343 (2012). https://doi.org/10.1364/OE.20.022334
31. V. Tiwari, N.S. Bisht, Spatial light modulators and their applications in polarization holography. In: Rosen, J. (ed.) Holography - Recent Advances and Applications. IntechOpen, London (2022). Chap. 1. https://doi.org/10.5772/intechopen.107110
32. A. Dreischuh, F. Grasbon, G.G. Paulus, F. Zacher, D. Neshev, H. Walther, Modulational instability of multiple-charged optical vortex solitons under saturation of the nonlinearity. Phys. Rev. E **60**, 7518–7524 (1999). https://doi.org/10.1103/PhysRevE.60.7518